

See discussions, stats, and author profiles for this publication at: <https://www.researchgate.net/publication/257837164>

# Engineering Hollow Nanocontainer Platform with Multifunctional Molecular Machines for Tumor-Targeted Therapy in Vitro and in Vivo.

ARTICLE in ACS NANO · OCTOBER 2013

Impact Factor: 12.88 · DOI: 10.1021/nn404676w · Source: PubMed

CITATIONS

56

READS

70

14 AUTHORS, INCLUDING:



Zhong Luo

Nanyang Technological University

48 PUBLICATIONS 903 CITATIONS

SEE PROFILE



Beilu Zhang

Michigan Technological Univeristy

9 PUBLICATIONS 213 CITATIONS

SEE PROFILE



Hong Yan

Agency for Science, Technology and Researc...

31 PUBLICATIONS 425 CITATIONS

SEE PROFILE



Liangliang Zhu

Nanyang Technological University

62 PUBLICATIONS 989 CITATIONS

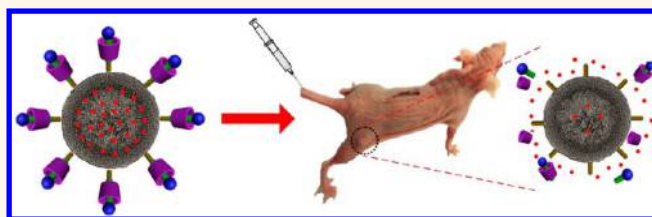
SEE PROFILE

# Engineering a Hollow Nanocontainer Platform with Multifunctional Molecular Machines for Tumor-Targeted Therapy *in Vitro* and *in Vivo*

Zhong Luo,<sup>†</sup> Xingwei Ding,<sup>‡</sup> Yan Hu,<sup>‡</sup> Shaojue Wu,<sup>†</sup> Yang Xiang,<sup>§</sup> Yongfei Zeng,<sup>†</sup> Beilu Zhang,<sup>‡</sup> Hong Yan,<sup>†</sup> Huacheng Zhang,<sup>†</sup> Liangliang Zhu,<sup>†</sup> Junjie Liu,<sup>‡</sup> Jinghua Li,<sup>‡</sup> Kaiyong Cai,<sup>‡,\*</sup> and Yanli Zhao<sup>†,‡,\*</sup>

<sup>†</sup>Division of Chemistry and Biological Chemistry, School of Physical and Mathematical Sciences, Nanyang Technological University, 21 Nanyang Link, Singapore 637371, <sup>‡</sup>Key Laboratory of Biorheological Science and Technology, Ministry of Education, College of Bioengineering, Chongqing University, Chongqing 400044, People's Republic of China, <sup>§</sup>Medical Research Center, Southwestern Hospital, The Third Military Medical University, Chongqing 400038, People's Republic of China, and <sup>‡</sup>School of Materials Science and Engineering, Nanyang Technological University, 50 Nanyang Avenue, Singapore 639798

**ABSTRACT** In order to selectively target malignant cells and eliminate severe side effects of conventional chemotherapy, biocompatible and redox-responsive hollow nanocontainers with tumor specificity were fabricated. The mechanized nanocontainers were achieved by anchoring mechanically interlocked molecules, *i.e.*, [2]rotaxanes, onto the orifices of hollow mesoporous silica nanoparticles *via* disulfide bonds as intermediate linkers for intracellular glutathione-triggered drug release. The [2]rotaxane employed was mainly composed of U.S. Food and Drug Administration approved tetraethylene glycol chains,  $\alpha$ -cyclodextrin, and folic acid. In this study, folate groups on the mechanized hollow nanocontainers act as both the tumor-targeting agents and stoppers of the [2]rotaxanes. Detailed investigations showed that anticancer drug doxorubicin loaded mechanized nanocontainers could selectively induce the apoptosis and death of tumor cells. The drug-loaded nanocontainers enhanced the targeting capability to tumor tissues *in vitro* and inhibited the tumor growth with minimal side effects *in vivo*. The present controlled and targeted drug delivery system paves the way for developing the next generation of nanotherapeutics toward efficient cancer treatment.



**KEYWORDS:** hollow mesoporous silica nanoparticles · *in vivo* · redox-responsive release · molecular machines · tumor-targeted therapy

Malignant tumors such as lung and breast tumors are the leading cause of human death worldwide, with an estimated 7.6 million deaths in 2008.<sup>1</sup> Although conventional chemotherapeutic strategies have been exploited for cancer treatment, healthy organs are also adversely affected due to severe toxicity of chemotherapeutics.<sup>2</sup> It is, therefore, urgent to develop novel and efficient therapeutic methods to selectively kill cancer cells for curing tumor illness, while with fewer side effects to healthy organs.<sup>2,3</sup> Nanotechnology presents a great potential to revolutionize cancer therapy by providing targeted drug delivery nanosystems to realize optimal treatments.<sup>2,3</sup> Mesoporous silica nanoparticles (MSNs), as one of the most promising therapeutic drug carriers, have been employed to fabricate responsive drug delivery

systems, mainly owing to their unique features of uniform mesopores, tunable pore sizes, large surface areas, and good biocompatibility *in vitro* and *in vivo*.<sup>4–8</sup> Since abundant silanol groups (Si-OH) on the surfaces of the nanoparticles are available for further modifications,<sup>4–8</sup> various types of MSN-based stimuli-responsive drug delivery systems have been developed.<sup>4–32</sup> These systems could be divided into three categories according to the capping agents functionalized on MSNs: (1) MSNs sealed by inorganic nanoparticles,<sup>9–13</sup> (2) MSNs capped by organic (bio)molecules and (bio)macromolecules,<sup>14–18,30–32</sup> and (3) MSNs mechanized with responsive molecular machines.<sup>19–29</sup> A key issue for these systems is how to “switch off” and “switch on” the mesopores in response to biological signals or external stimuli for controlled drug delivery.<sup>4–8</sup>

\* Address correspondence to zhaoyanli@ntu.edu.sg; kaiyong\_cai@cqu.edu.cn.

Received for review September 6, 2013 and accepted October 15, 2013.

Published online October 16, 2013 10.1021/nn404676w

© 2013 American Chemical Society

Mechanized MSNs are usually achieved by immobilization of functional supramolecular machines,<sup>19–22</sup> monolayer nanovalves,<sup>23–25</sup> and artificial interlocked molecules<sup>26,27</sup> onto the surfaces of MSNs. They have been exploited to store and release therapeutic agents on account of their good drug encapsulation capability and high sensitivity to external stimuli.<sup>5</sup> For instance, Stoddart and Zink functionalized (supra)molecular machines onto MSNs by employing switchable [2]rotaxanes or [2]pseudorotaxanes as gates to control cargo release under external stimuli.<sup>5,19–22,26,27</sup> We also constructed redox-, pH-, enzyme-, and light-responsive release systems based on MSNs for controlled and targeted drug delivery.<sup>28–32</sup> A classic model of [2]rotaxane-functionalized MSNs is usually composed of four parts:<sup>5</sup> (1) linear stalks, which are tailored onto the surfaces of MSNs, (2) movable macrocyclic rings, such as tetracationic cyclophanes, crown ethers, cucurbiturils, and cyclodextrins, which are threaded onto the stalks by specific molecular recognitions, (3) cleavable bonds or stimuli-responsive binding sites, which are introduced onto stalks to control the movement of rings, thus leading to opening or closure of the mesopores, and (4) stoppers, which are conjugated onto the termini of stalks for completing [2]rotaxanes on MSNs. All components employed in the fabrication of molecular machines onto MSNs are highly modular for specific requirements.<sup>5,19–27</sup> However, previously reported mechanized MSNs were not endowed with tumor-specific capability, and almost all the studies did not involve in the investigation and evaluation of MSN-based delivery systems *in vivo*. Thus, it is important to accumulate proof of controlled and targeted intracellular drug delivery using mechanized MSNs, interaction mechanisms between tumor cells and mechanized MSNs, and animal curative effects of mechanized MSN-based drug release systems for potential clinical applications.

Herein, we functionalized novel [2]rotaxanes onto hollow mesoporous silica nanocontainers (HMSNs) by using disulfide bonds as intermediate linkers and investigated their applications for controlled and targeted drug delivery *in vitro* and *in vivo* (Figure 1). HMSNs were employed as drug storage nanocontainers with enhanced drug loading capacity as compared with conventional MSNs. Multifunctional [2]rotaxanes on HMSNs were fabricated by using the biocompatible products tetraethylene glycol (TEG),  $\alpha$ -cyclodextrin ( $\alpha$ -CD), and folic acid (FA). Briefly, HMSNs were first functionalized with disulfide bond containing amino groups. After that, a TEG derivative was immobilized onto the above nanoparticles, acting as a dumbbell-like component of the [2]rotaxane. A movable  $\alpha$ -CD ring was threaded onto the TEG unit with high complexation affinity between the linear  $-(CH_2-CH_2O)_4-$  chain of TEG and the hydrophobic cavity of  $\alpha$ -CD.<sup>22</sup> The  $\alpha$ -CD rings on the HMSN surface

could physically block the loaded drugs within the hollow pores on account of the unique three-dimensional structure.<sup>16,21</sup> Finally, [2]rotaxane-functionalized HMSNs were achieved by anchoring FA onto the end of the TEG chain *via* click chemistry. The FA unit with 2-amino 4-hydroxyl pteridin structure as well as three  $-NH-$  groups (red dashed circles in Figure 1A) could prevent  $\alpha$ -CD from dethreading.<sup>5,29</sup> Thus, the FA unit acts as both the stopper of [2]rotaxane on the HMSN surface and a targeting agent toward tumor cells. Since the disulfide bond linkage can be cleaved by intracellular reducing agents, *i.e.*, glutathione (GSH), removal of the [2]rotaxane capping agents on the HMSN surface leads to the release of loaded drugs. Here, we demonstrated that [2]rotaxane-mechanized HMSNs were a biocompatible and efficient redox-responsive drug delivery system with tumor specificity *in vitro* and *in vivo*.

## RESULTS AND DISCUSSION

**Preparation of Mechanized HMSNs.** The precursors of S-(2-pyridylthio)-cysteamine hydrochloride, *p*-toluenesulfonate tetraethylene glycol azide (Tos-TEG-N<sub>3</sub>), and acetylated folic acid (FA-C $\equiv$ C) were first synthesized according to previous reports with slight modifications,<sup>22,33</sup> which were described in the Supporting Information (SI). Successful synthesis of those molecules was confirmed by nuclear magnetic resonance (NMR) spectroscopy (Figure S1 in the SI) and mass spectroscopy (MS) (Figure S2 in the SI). It is interesting to note that correlative cross-peaks appeared (red arrows in Figure S3 of the SI) when the  $\alpha$ -CD ring was threaded onto the OH-TEG-OH molecule in a DMSO/D<sub>2</sub>O mixture solution. The observation indicates that the linear  $-(CH_2-CH_2O)_4-$  chain of the TEG molecule was included in the  $\alpha$ -CD cavity, suggesting that the inclusion complexation between the  $\alpha$ -CD ring and the TEG molecule could also be achieved on the HMSN surface. Then, HMSNs were prepared by using a template method according to previous reports with some changes (Figure S4 in the SI).<sup>34</sup> The synthesized HMSNs displayed a uniform hollow structure and well-defined mesoporous shell with an average diameter of  $155 \pm 20$  nm (Figure 2a,c). The average thickness of the shell was  $20 \pm 2.5$  nm. It was reported that nanoscale drug delivery systems smaller than 200 nm could be eliminated from the body after long-term circulation *in vivo*.<sup>2,35</sup> Consequently, the obtained HMSNs could be exploited as promising drug nanocarriers.

Mechanized HMSNs were finally obtained after loading with the anticancer drug doxorubicin hydrochloride (DOX) and modifications with multifunctional  $\alpha$ -CD-based [2]rotaxane (Figure 1A and Figure 2b,d). The detailed grafting procedure and reaction principle are described in the SI. Briefly, the synthetic procedure includes six steps: (1) HMSNs were first modified with a

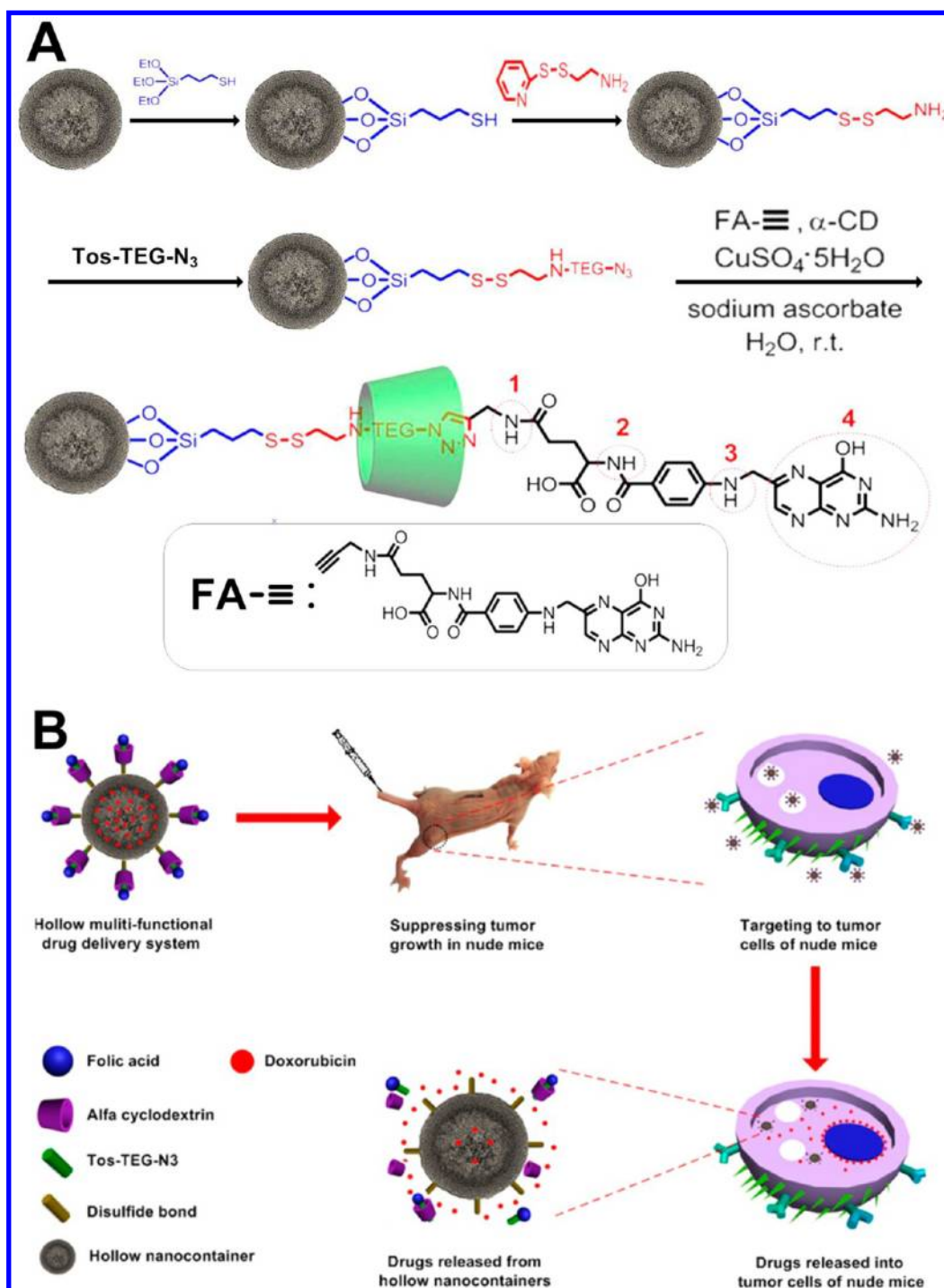
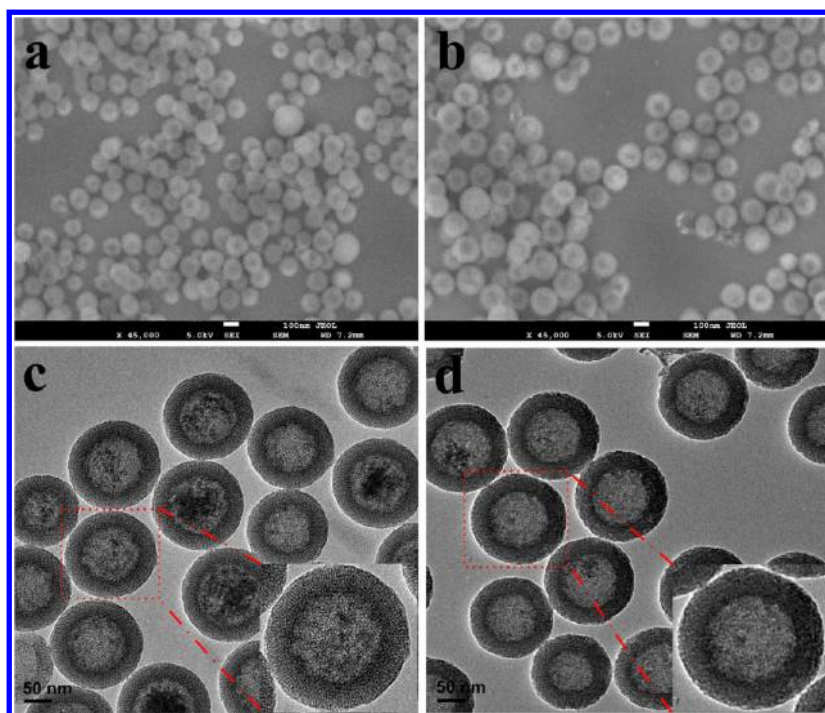


Figure 1. (A) Fabrication of multifunctional [2]rotaxanes onto the orifice of HMSNs. (B) Redox-responsive mechanized HMSNs with tumor specificity for drug delivery *in vitro* and *in vivo*.

sulfhydryl unit (–SH) using mercaptopropyltrimethoxysilane,<sup>11,12</sup> denoted as HMSNs-SH; (2) HMSNs were functionalized with a disulfide bond containing amino groups through the disproportionation reaction between HMSNs-SH and S-(2-pyridylthio)cysteamine hydrochloride,<sup>11</sup> denoted as HMSNs-S-S-NH<sub>2</sub>; (3) Tos-TEG-N<sub>3</sub> was immobilized onto the orifices of MSNs-S-S-NH<sub>2</sub> by the reaction between a toluenesulfonate group and an amino group,<sup>22</sup> denoted as HMSNs-S-S-NH-TEG-N<sub>3</sub>;

(4) model drug DOX or fluorescein isothiocyanate (FITC) was loaded into HMSNs-S-S-NH-TEG-N<sub>3</sub> *via* diffusion, denoted as HMSNs-S-S-NH-TEG-N<sub>3</sub>@DOX or HMSNs-S-S-NH-TEG-N<sub>3</sub>@FITC; (5) the α-CD ring was threaded onto the TEG chain on the nanoparticle surface,<sup>22</sup> denoted as HMSNs-S-S-NH-TEG-N<sub>3</sub>/α-CD@DOX or HMSNs-S-S-NH-TEG-N<sub>3</sub>/α-CD@FITC; and finally (6) acetylated folic acid (FA-C≡C) was anchored onto the end of the TEG chain to achieve the mechanized HMSNs *via* click chemistry





**Figure 2.** Morphology of HMSNs and mechanized HMSNs. SEM images of (a) bare HMSNs and (b) mechanized HMSNs (HMSNs-S-S-NH-TEG-FA/ $\alpha$ -CD), scale bar: 100 nm; TEM images of (c) bare HMSNs and (d) mechanized HMSNs (HMSNs-S-S-NH-TEG-FA/ $\alpha$ -CD), scale bar: 50 nm.

between azide and alkynyl units, denoted as HMSNs-S-S-NH-TEG-FA/ $\alpha$ -CD@DOX or HMSNs-S-S-NH-TEG-FA/ $\alpha$ -CD@FITC.

To monitor the modification processes, the samples were fully characterized by scanning electron microscopy (SEM), transmission electron microscopy (TEM), Brunauer–Emmett–Teller (BET) surface area measurements, Barrett–Joyner–Halenda (BJH) pore size distribution analysis, Fourier transform infrared spectroscopy (FTIR), fluorescamine spectroscopy, zeta potential measurements, and thermogravimetric analysis (TGA). The SEM and TEM images confirmed that both HMSNs and mechanized HMSNs displayed uniform hollow structures with an average diameter of  $155 \pm 20$  nm and average shell thickness of  $20 \pm 2.5$  nm (Figure 2a–d). However, the mesoporous structure of mechanized HMSNs (HMSNs-S-S-NH-TEG-FA/ $\alpha$ -CD) cannot be clearly observed compared with bare HMSNs as a result of the surface functionalization (Figure 2b,d).<sup>32,36</sup> The BET surface areas of nanoparticles decreased from  $1291.7 \text{ m}^2 \text{ g}^{-1}$  to  $416.5 \text{ m}^2 \text{ g}^{-1}$  after HMSNs were mechanized with [2]rotaxane (Figure S5 and Table S1 in the SI). The BJH pore sizes of nanoparticles also decreased after the grafting process (Figure S5 and Table S1 in the SI).<sup>37</sup> These results suggest that the mesopores (around 3.8 nm in diameter) of mechanized HMSNs were capped by  $\alpha$ -CD-based [2]rotaxane. FTIR spectra (Figure S6 in the SI) further demonstrated that HMSNs-S-S-NH-TEG-FA/ $\alpha$ -CD was successfully synthesized after step-by-step reactions. Fluorescamine spectra (Figure S7 in the SI) proved that HMSNs-S-S-NH<sub>2</sub> and HMSNs-S-S-NH-TEG-N<sub>3</sub> were

prepared. Fluorescamine detection is based on the fact that primary amine groups ( $-\text{NH}_2$ ) can react with fluorescamine to generate significant fluorescence.<sup>32</sup> Thus, the fluorescence intensity indicates the amount of primary amine groups on the nanoparticles. The fluorescence intensity of HMSNs-S-S-NH-TEG-N<sub>3</sub> became much lower than that of HMSNs-S-S-NH<sub>2</sub>, since the primary groups ( $-\text{NH}_2$ ) were consumed in the grafting reaction. Zeta potential indicated that  $-\text{SH}$ ,  $-\text{NH}_2$ ,  $-\text{N}_3$ , and  $-\text{OH}$  from  $\alpha$ -CD were introduced onto the surface of HMSNs, since the charge values of the samples varied after each step of the modification (Table S2 in the SI).<sup>7</sup> Furthermore, TGA confirmed that around 20 wt % of DOX was loaded into the mechanized HMSNs (Figure S8 in the SI), a loading value that is much higher than that of conventional MSNs (less than 10 wt %). The amount of other functional species immobilized onto the surface of HMSNs was measured quantitatively as well (Figure S8 in the SI).

**Redox-Responsive Drug Release.** The release behavior of an anticancer drug from DOX-loaded mechanized HMSNs under intracellular redox stimuli was investigated. In this study, after loading DOX into mechanized HMSNs, HMSNs-S-S-NH-TEG-FA/ $\alpha$ -CD@DOX was exposed to neutral Tris buffers containing various amounts of intracellular reducing agent, *i.e.*, GSH. Real-time release behavior of the system was monitored using a fluorescence spectrometer (Figure 3a). At physiological conditions (Tris buffers), a negligible amount of DOX was leaked from HMSNs-S-S-NH-TEG-FA/ $\alpha$ -CD@DOX within 2 h, indicating good capping efficiency of  $\alpha$ -CD-based

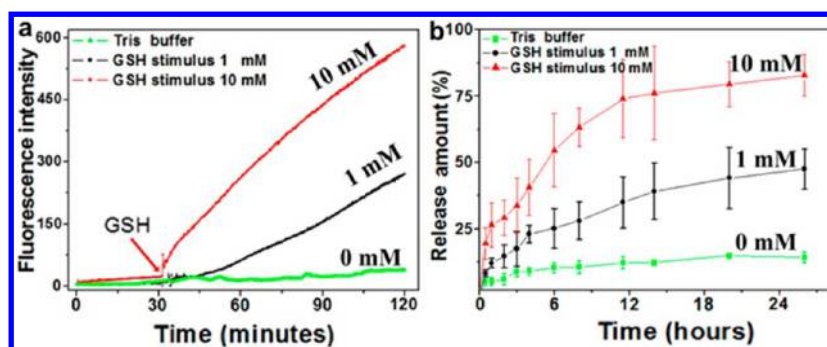


Figure 3. Redox-responsive release profiles of DOX from the mechanized HMSNs. (a) Real-time release profiles over 120 min and (b) long-term release profiles over 26 h.

[2]rotaxane on the nanoparticle surface.<sup>19,21,28,29</sup> In comparison, when mechanized HMSNs were exposed to 1 mM and 10 mM GSH solutions in Tris buffer for redox-triggered release, the fluorescence intensity of DOX drastically increased to 285 (au) and 590 (au), respectively (Figure 3a). This phenomenon could be explained by GSH causing the cleavage of the disulfide bonds due to its reducibility, thus leading to the removal of the [2]rotaxane capping agents from the nanoparticle surface for quick cargo release.<sup>38,39</sup> It has been also reported that GSH is extensively distributed in the cytoplasm of tumor cells.<sup>40,41</sup> To some extent, the DOX release rate from mechanized HMSNs was dependent on the concentration of the reducing agent.<sup>38,39</sup> These results indicate that the HMSNs-S-S-NH-TEG-FA/ $\alpha$ -CD@DOX drug delivery system was highly sensitive to the redox stimulus provided by GSH.

To further investigate the long-term redox-triggered drug release behavior of mechanized HMSNs, the system was incubated with 1 mM and 10 mM GSH solutions for 26 h, respectively. At physiological conditions, the leakage amount of DOX from mechanized HMSNs still remained at a low level (nearly 10%) when incubated for more than one day (Figure 3b), further demonstrating that the [2]rotaxane capping agents could keep the loaded anticancer drugs within the nanocontainers.<sup>38,39</sup> A possible reason for the drug leakage was that some DOX might be adsorbed onto the surface of HMSNs or reside in the ditches among the [2]rotaxane capping agents, which was released quickly into the buffer solution *via* free diffusion within 4 h.<sup>28–32,38,39</sup> In contrast, the released amount of DOX increased to over 50% and 85% when the delivery system was treated with 1 mM and 10 mM GSH solutions for 26 h, respectively. The mechanism is that the disulfide bonds between the [2]rotaxane capping agents and HMSNs were stable at physiological conditions, leading to robust blocking of the mesopores by the [2]rotaxanes (off state). When the delivery system was exposed to a reductive environment, the disulfide bonds would be cleaved, resulting in the removal of the [2]rotaxane capping agents from the HMSN surface as well as the uncapping of the mesopores for the DOX

release (on state).<sup>38,39</sup> Moreover, the release profiles of DOX-loaded mechanized HMSNs under endosome-mimetic circumstances (pH = 5.0) were also investigated, since the delivery system would be trapped inside the endosome after being endocytosed by HeLa cells. As shown in Figure S9 of the SI, nearly 13% of DOX was leaked from mechanized HMSNs after incubation for 1 day, which was similar to the release profiles at physiological conditions. The results further demonstrated that the [2]rotaxane capping agents could maintain the loaded anticancer drugs within the nanocontainers even under acidic conditions.

**Interactions of Mechanized HMSNs with Tumor Cells.** To evaluate the interaction between mechanized HMSNs (HMSNs-S-S-NH-TEG-FA/ $\alpha$ -CD) and tumor cells *in vitro*, TEM was first used to monitor the distribution of HMSNs and HMSNs-S-S-NH-TEG-FA/ $\alpha$ -CD within HeLa cells.<sup>42,43</sup> The cells on tissue culture polystyrene plates (TCPP) were used as the control group. It was observed that HeLa cells treated with the nanoparticles still displayed a well-spread morphology compared with the control group (Figure 4b,c vs 4a). The cell membranes and nuclei were intact and distinct. These results indicate that both HMSNs and HMSNs-S-S-NH-TEG-FA/ $\alpha$ -CD were of good biocompatibility,<sup>42,43</sup> which was also supported by the cell viability assay of the nanoparticles (Figure S10 in the SI). Moreover, the nanoparticles entered into the cytoplasm without any interactions with the cell nuclei. This observation is consistent with previous studies.<sup>42,43</sup> Interestingly, the endocytosed amount of HMSNs-S-S-NH-TEG-FA/ $\alpha$ -CD by HeLa cells was much higher than that of HMSNs. It could be interpreted that the targeting ligands, FA units, in HMSNs-S-S-NH-TEG-FA/ $\alpha$ -CD specifically interacted with tumor cells, thus improving its cellular uptake. Furthermore, we also found that an endosome was formed to contain the nanoparticles *in situ* after they were endocytosed by cells (Figure 4b vs 4e, red line, and Figure S11 in the SI).<sup>30</sup> The formation of the endosome is a cellular immune response for self-protection when exogenous species come into cells.<sup>44</sup> Our previous studies have confirmed that internalized nanoparticles with positive charges could escape from

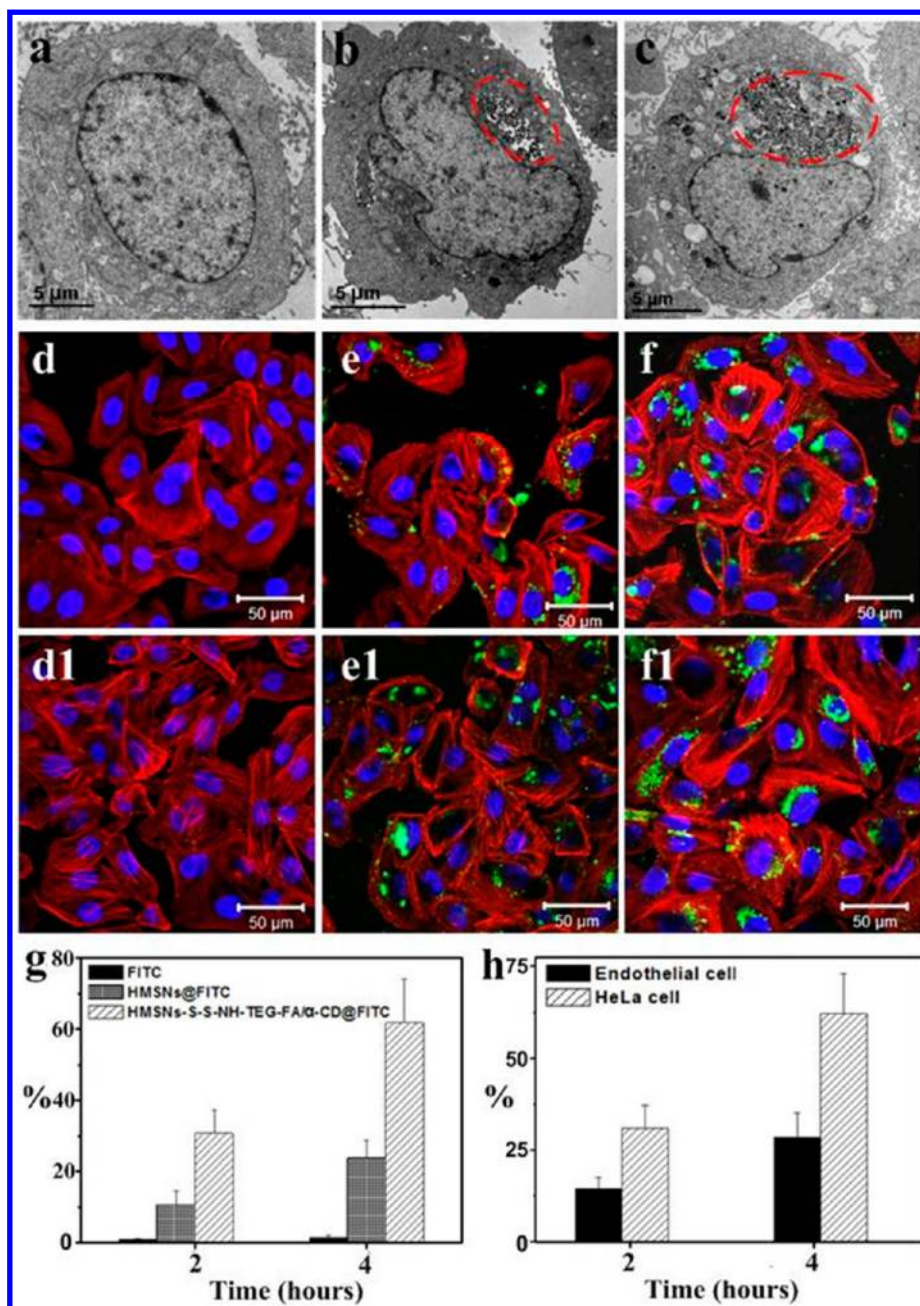


**Figure 4.** TEM images showing untreated HeLa cells (a, control group) and the distributions of endocytosed HMSNs (b) and mechanized HMSNs (c) within HeLa cells after 12 h. Representative CLSM images of free FITC (d and d1), HMSNs@FITC (e and e1), and HMSNs-S-S-NH<sub>2</sub>-TEG-FA/α-CD@FITC (f and f1) endocytosed by HeLa cells for 12 and 24 h, respectively. Scale bar: 50 μm. Red: cytoskeleton, blue: cell nuclei, green: FITC-labeled nanoparticles. (g) Quantitative flow cytometry analysis showing the percentage of HeLa cells with fluorescence after incubation with FITC, HMSN@FITC, and HMSNs-S-S-NH<sub>2</sub>-TEG-FA/α-CD@FITC, respectively. (h) Quantitative flow cytometry analysis showing the percentage of HeLa cells and endothelial cells with fluorescence after incubation with HMSNs-S-S-NH<sub>2</sub>-TEG-FA/α-CD@FITC, n = 6.

the endosome owing to the cellular “sponge effect”.<sup>28,45</sup> After that, the escaped nanoparticles would enter the cytoplasm of tumor cells and be exposed to the reductive environment provided by intracellular GSH.

Second, confocal laser scanning microscopy (CLSM) was utilized to quantitatively evaluate the amount of nanoparticles endocytosed by tumor cells.<sup>16,30,43,45</sup> FITC was loaded into bare HMSNs and mechanized HMSNs, denoted as HMSNs@FITC and HMSNs-S-S-NH-

TEG-FA/α-CD@FITC, respectively. After being incubated with HMSNs@FITC and HMSNs-S-S-NH-TEG-FA/α-CD@FITC for 12 and 24 h, respectively, HeLa cells were fixed and stained with dyes to reveal their cell morphology *in vitro*. CLSM observation demonstrated that, after taking up the nanoparticles, HeLa cells displayed well-spreading morphologies compared with the controlled group with FITC only (Figure 4e,f vs 4d; 4e1,f1 vs 4d1). These cell nuclei (blue) and cell



cytoskeletons (red) also remained intact with regular structures. The internalized nanoparticles with green fluorescence were mainly located in the cytoplasm, without penetration into the cell nucleus.<sup>30,43,45</sup> Interestingly, the endocytosis efficiency of the nanoparticles increased with the incubation time (Figure 4e vs 4e1; 4f vs 4f1). Among them, HMSNs-S-S-NH-TEG-FA/ $\alpha$ -CD@FITC displayed higher cell internalization efficiency than that of HMSNs after incubation for 12 and 24 h, respectively (Figure 4f vs 4e; 4f1 vs 4e1). For quantitative analysis, mean fluorescence intensity (MFI) per cell was measured to investigate the cell uptake ability. The MFI per cell with HMSNs-S-S-NH-TEG-FA/ $\alpha$ -CD@FITC was 2.5-fold and 1.9-fold higher than that of HMSNs after incubation for 12 and 24 h, respectively (Figure S12 in the SI). The mechanism is that FA units on the surface of HMSNs-S-S-NH-TEG-FA/ $\alpha$ -CD@FITC could improve the internalization efficiency of the nanoparticles through specific receptor-mediated endocytosis.<sup>46</sup> In addition, the interaction between the nanoparticles and fetal bovine serum (FBS) confirmed that the adsorption amount of FBS onto HMSNs-S-S-NH-TEG-FA/ $\alpha$ -CD was much lower than that of HMSNs. It could be interpreted that the TEG units on HMSNs-S-S-NH-TEG-FA/ $\alpha$ -CD prevent the protein attachment to the nanoparticle surface (Table S3 in the SI), which ensured that the FA units targeted cancer cells. As shown in Tables S4 and S5 of the SI, although the FBS protein adsorption on the nanoparticle could increase the nanoparticle sizes, it still did not result in nanoparticle aggregation.

Third, we quantified the targeted uptake ability of HMSNs-S-S-NH-TEG-FA/ $\alpha$ -CD@FITC by comparing tumor cells with normal cells through a flow cytometry assay.<sup>30,32</sup> FITC was employed as the marker for intracellular tracing. After incubation with HMSNs-S-S-NH-TEG-FA/ $\alpha$ -CD@FITC for 2 and 4 h, the percentage of HeLa cells with fluorescence was around 2.86 times and 2.58 times higher than that of HeLa cells incubated with HMSNs@FITC for the same duration, respectively (Figure 4g). It is noted that HeLa cells hardly endocytose free FITC, since such a small molecule in solution could not easily permeate the cell membranes.<sup>3,47</sup> In order to further investigate the targeting capability of mechanized HMSNs, tumor cells (HeLa cells) and normal cells (endothelial cells) were incubated with HMSNs-S-S-NH-TEG-FA/ $\alpha$ -CD@FITC, respectively. We found that the uptake efficiency of HMSNs-S-S-NH-TEG-FA/ $\alpha$ -CD@FITC by HeLa cells was nearly two times higher than that of endothelial cells (Figure 4f). The significant difference could be explained by the fact that the amount of folate receptors on tumor cells was much higher than that on normal cells, which facilitates specific receptor-mediated endocytosis of HMSNs-S-S-NH-TEG-FA/ $\alpha$ -CD@FITC by HeLa cells.<sup>46</sup>

**Inhibitory Effects of DOX-Loaded Mechanized HMSNs on the Activity of Tumor Cells *in Vitro*.** To apply DOX-loaded

mechanized HMSNs for *in vivo* tumor therapy, we first investigated their inhibiting effects on the growth of tumor cells *in vitro*. We initially visualized the cell morphology by CLSM after the cells were treated with DOX and DOX-loaded nanoparticles for 24 h, respectively.<sup>30,32,45,47</sup> In this study, DOX was trapped into bare HMSNs and mechanized HMSNs, denoted as HMSNs@DOX and HMSNs-S-S-NH-TEG-FA/ $\alpha$ -CD@DOX, respectively. HeLa cells incubated with TCPP and HMSNs displayed oval or round nuclei with discernible boundaries (Figure 5a and b). However, the cell nuclei deformed and ruptured after treatment with DOX, HMSNs@DOX, and HMSNs-S-S-NH-TEG-FA/ $\alpha$ -CD@DOX for 24 h, respectively (Figure 5c–e). These observations indicate that the cells were in an apoptotic stage.<sup>45</sup> Interestingly, the cell nuclei displayed red-blue mixed color after incubation with DOX or DOX-loaded nanoparticles. The reason might be that pure DOX or released DOX from mechanized HMSNs could cleave the double-stranded DNA in the cell nuclei.<sup>16</sup> On the other hand, a small amount of DOX (red color) remained in the cytoplasm after HeLa cells were incubated with HMSNs-S-S-NH-TEG-FA/ $\alpha$ -CD@DOX. This observation could be interpreted that DOX was released into the cytoplasm in the presence of intracellular reducing agents. The released DOX had no interaction with the cell nucleus at the time. All these results confirmed that HMSNs-S-S-NH-TEG-FA/ $\alpha$ -CD@DOX could be endocytosed by HeLa cells and then release DOX into cytoplasm triggered by intracellular reducing agents, *i.e.*, GSH. Finally, the released DOX specifically affiliates with DNA of tumor cells to induce apoptosis and cell death.

Then, we quantitatively evaluated the inhibition effects of free DOX and DOX-loaded nanoparticles on the growth of HeLa cells using the methylthiazolyl tetrazolium (MTT) assay.<sup>28</sup> As shown in Figure S13 of the SI, the growth of tumor cells was severely inhibited after incubation with DOX, HMSNs@DOX, and HMSNs-S-S-NH-TEG-FA/ $\alpha$ -CD@DOX, compared with that of TCPP for 24 h. The inhibition efficiency of HMSNs-S-S-NH-TEG-FA/ $\alpha$ -CD@DOX on the growth of HeLa cells was similar to that of HMSNs@DOX over 6 and 12 h. It could be interpreted that DOX was released quickly from HMSNs@DOX to inhibit the growth of HeLa cells in the initial stage. In contrast, the release of DOX from HMSNs-S-S-NH-TEG-FA/ $\alpha$ -CD@DOX would only occur after the nanoparticles were endocytosed by HeLa cells and triggered by intracellular reductive GSH. The viability of HeLa cells after incubation with HMSNs-S-S-NH-TEG-FA/ $\alpha$ -CD@DOX over 24 h was lower than that of HMSNs@DOX, which could be attributed to the fact that the FA units facilitated cellular uptake of HMSNs-S-S-NH-TEG-FA/ $\alpha$ -CD@DOX via folate receptor-mediated endocytosis. Then, DOX was released into the cytoplasm induced by intracellular reductive GSH, resulting in high inhibition effects on the cell growth.<sup>46</sup>



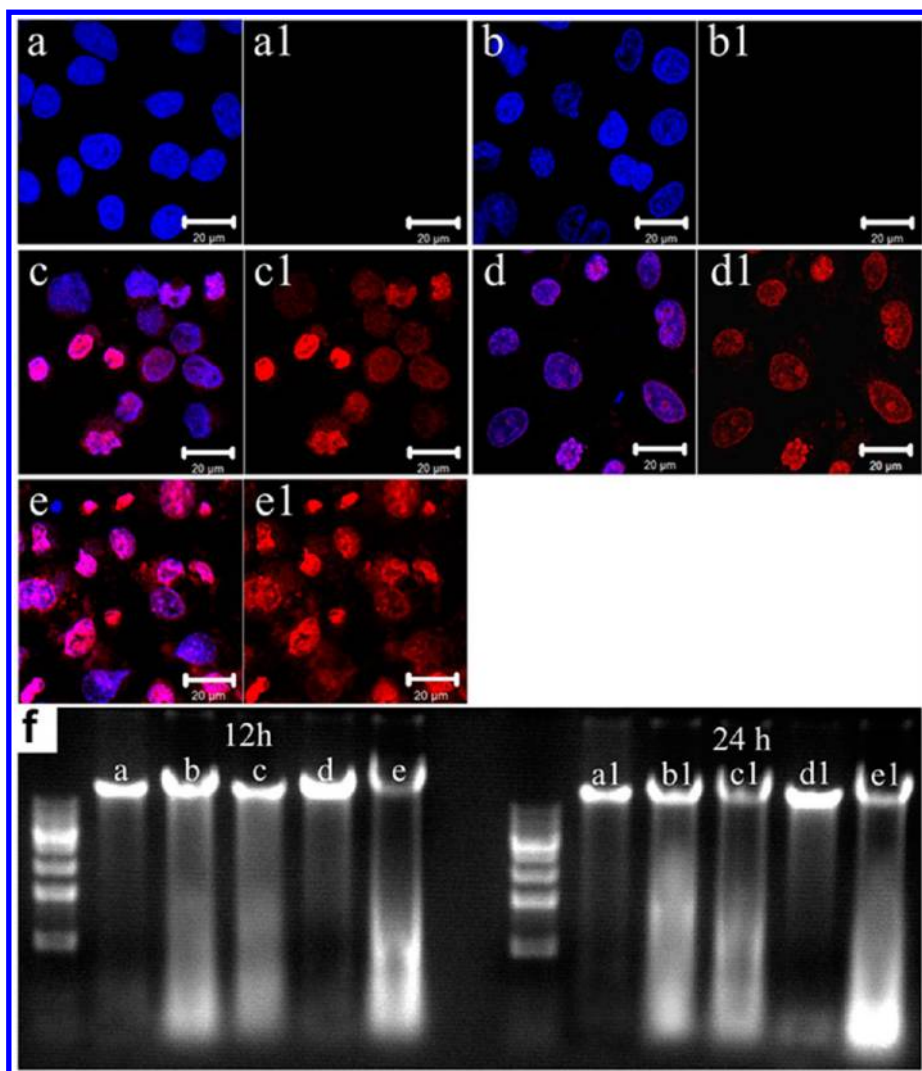


**Figure 5.** Representative CLSM images of HeLa cells incubated with TCPP (a and a1, as the control group), HMSNs (b and b1), DOX (c and c1), HMSNs@DOX (d and d1), and HMSNs-S-S-NH-TEG-FA/α-CD@DOX (e and e1) for 24 h, respectively. Scale bar: 20 μm. Merged figures from H33258 and DOX channels: a–e; DOX channels: a1–e1. Red: DOX; blue: cell nuclei. (f) DNA fragmentation assay (apoptosis) after treatment with TCPP (lanes a and a1), DOX (lanes b and b1), MSNs@DOX (lanes c and c1), HMSNs (lanes d and d1), and HMSNs-S-S-NH-TEG-FA/α-CD@DOX (lanes e and e1) for 12 and 24 h, respectively.

Moreover, the viability of HeLa cells treated with pure DOX was the lowest one among all three groups. A possible reason is that pure DOX could be rapidly dissolved into the culture medium, leading to a high transient DOX concentration to quickly inhibit the growth of HeLa cells at the initial stage.<sup>28</sup>

We further performed a DNA ladder analysis to reveal the apoptosis mechanism of the cells after being treated with DOX and DOX-loaded nanoparticles (Figure 5f).<sup>30,45,48</sup> DOX was reported to interact with DNA and topoisomerase II in tumor cell nuclei to result in apoptosis by inducing DNA fragmentation.<sup>16,49,50</sup> As shown in Figure 5f, DNA fragmentation was not observed when HeLa cells were incubated on TCPP or with bare HMSNs for 12 and 24 h, respectively (Figure 5f: lanes a vs d and a1 vs d1). The phenomenon confirms that HMSNs had a good biocompatibility and did not destroy the DNA structures within

cells.<sup>30–32,48</sup> In contrast, DNA fragmentation was visible when the cells were incubated with DOX, HMSNs@DOX, and HMSNs-S-S-NH-TEG-FA/α-CD@DOX for 12 and 24 h, respectively (Figure 5g: lanes c–e and c1–e1). Moreover, HeLa cells treated with HMSNs-S-S-NH-TEG-FA/α-CD@DOX presented a higher intensity of fragmentation than those of other groups. The mechanism is that the [2]rotaxane capping agents on the HMSN surfaces could efficiently prevent DOX release from the nanocontainers until they were endocytosed by HeLa cells and distributed into the cytoplasm. Under intracellular reductive conditions, the disulfide bonds between the [2]rotaxane capping agents and HMSNs were cleaved. Then, the loaded DOX was released into the cytoplasm, leading to efficient cancer cell death. The HMSNs@DOX nanoparticles lacked cleavable capping agents on the surface, so that the loaded DOX could be partially leaked out even before the nanoparticles were

internalized by tumor cells. Therefore, the efficiency of the apoptosis induced by HMSNs@DOX was lower than that by HMSNs-S-S-NH-TEG-FA/ $\alpha$ -CD@DOX.<sup>30,45,48</sup> On the other hand, the folate targeting units on HMSNs-S-S-NH-TEG-FA/ $\alpha$ -CD@DOX played a key role in facilitating receptor-mediated endocytosis, further enhancing the efficiency of tumor cell apoptosis and death.<sup>46</sup>

**Curative Effects of DOX-Loaded Mechanized HMSNs on Tumor *in Vivo*.** To finally investigate curative effects of DOX-loaded mechanized HMSNs on tumor *in vivo*, tumor

models on nude mice were established by injection of HeLa cells into subcutaneous tissues.<sup>51</sup> After injection for 1 week, nude mice (around 19–20 g) with similar tumor size were utilized to carry out the studies.

We periodically measured the mouse weights after tail injection of DOX and DOX-loaded nanoparticles. The mice treated with saline were used as the control group. Every group has six duplicate mice samples ( $n = 6$ ). In the initial stage, the weights of nude mice were recorded to be approximately  $19.3 \pm 0.5$  g. All the

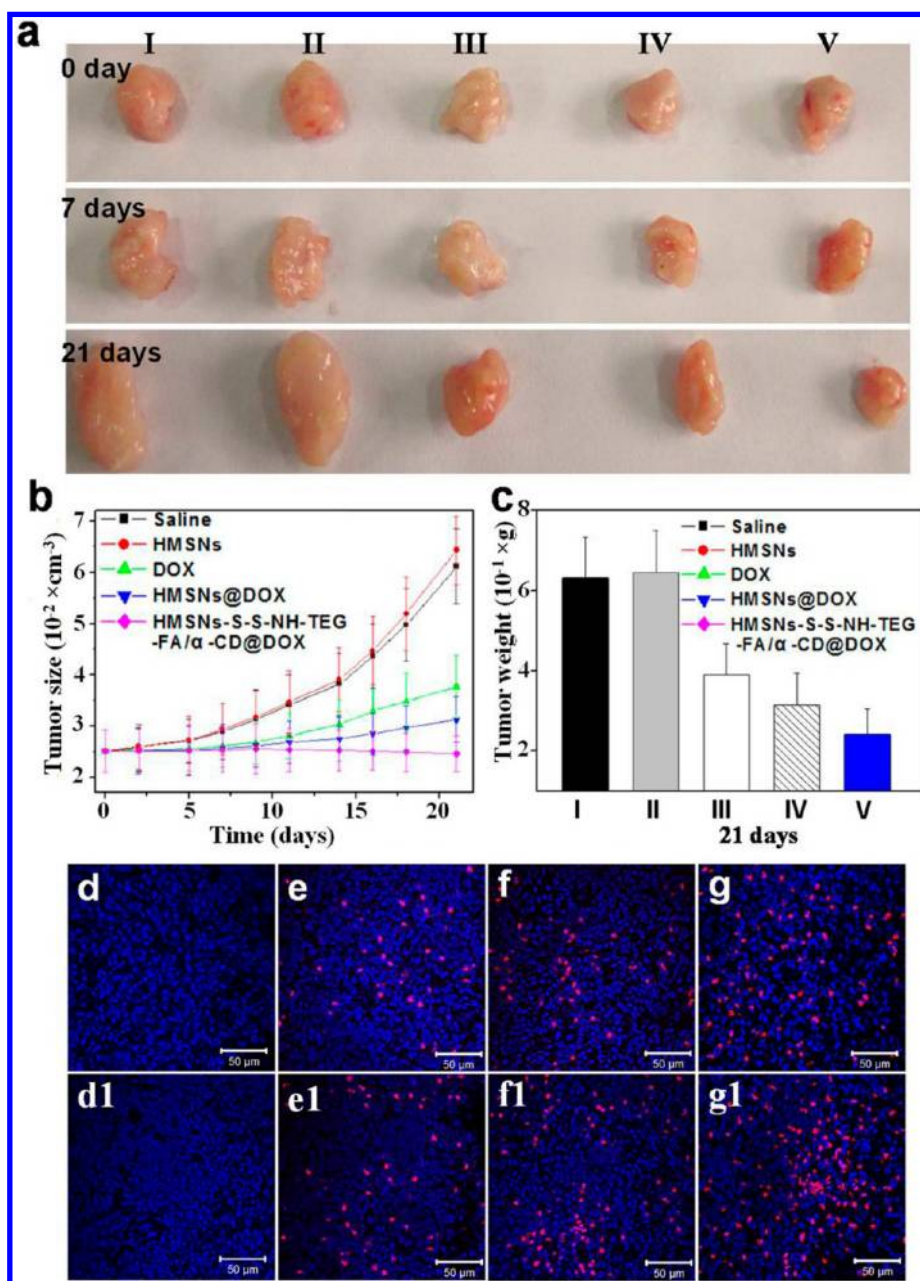


**Figure 6.** (a) Representative images of tumor tissues when treated with saline (I, control group), HMSNs (II), DOX (III), HMSNs@DOX (IV), and HMSNs-S-S-NH-TEG-FA/ $\alpha$ -CD@DOX (V) for 0 day, 7 days, and 21 days, respectively. Scale bar: 1 cm. (b) Real-time observation of tumor sizes by digital vernier caliper *in vivo* after treatment with these samples. Error bars represent means  $\pm$  standard deviation (SD) for  $n = 6$ ,  $*p < 0.05$ ,  $**p < 0.01$ . (c) Final weights of tumor tissues after treatment for 21 days. Error bars represent means  $\pm$  SD for  $n = 6$ ,  $*p < 0.05$ ,  $**p < 0.01$ . Histological observation of tumor tissues, using the tunnel method, after treatment with HMSNs (d and d1), DOX (e and e1), HMSNs@DOX (f and f1), and HMSNs-S-S-NH-TEG-FA/ $\alpha$ -CD@DOX (g and g1) for 7 and 21 days, respectively. Red: apoptosis DNA; blue: cell nuclei.

injections were operated three times per week. As shown in Figure S14 of the SI, the mice still maintained their weight around 20 g after injection with DOX and feeding for 21 days. However, the average weights of the mice treated with saline, HMSNs, HMSNs@DOX, and HMSNs-S-S-NH-TEG-FA/ $\alpha$ -CD@DOX increased to 24.7, 24.4, 23.8, and 22.4 g, respectively. The results indicate that HMSNs had a good biocompatibility and could reduce the side effects of DOX to nude mice when they were utilized as drug carriers.<sup>52–54</sup>

We then measured the tumor sizes at fixed time intervals in order to investigate the tumor growth after injection with DOX and DOX-loaded nanoparticles (Figure 6a). Quantitative analysis showed that *in vivo* tumor sizes increased upon feeding time after treating with saline, HMSNs, DOX, and HMSNs@DOX, respectively. As compared with the control groups of saline (negative) and HMSNs (positive), the growth of tumor sizes was inhibited when treated with DOX and HMSNs@DOX.<sup>52–54</sup> Curative effects of HMSNs@DOX on nude mice were better than that of pure DOX. Meaningfully, the nude mice treated with HMSNs-S-S-NH-TEG-FA/ $\alpha$ -CD@DOX showed much better curative effects than those of other groups. HMSNs-S-S-NH-TEG-FA/ $\alpha$ -CD@DOX could efficiently inhibit the growth of tumors after curing for 21 days (Figure 6b). The inhibition was also supported by the measurement of the final tumor tissue weight (Figure 6c). All results indicate that pure DOX could not easily reach tumor sites and interact with tumor cells *in vivo*.<sup>2</sup> After injection, DOX could only retain a transient high plasma drug concentration for a short time. It caused some damage or severe side effects to the normal cells and tissues *in vivo*.<sup>51</sup> Then, free DOX was quickly distributed into other tissue organs, lost its bioactivity, and was finally excreted out of body *via* blood circulation and metabolism.<sup>51</sup> To some extent, HMSNs@DOX retains a blood drug concentration at a certain level through sustained release when they were injected. Although HMSNs@DOX might relieve some side effects of DOX on the body, DOX still cannot be delivered to the target tumor tissues.<sup>51</sup> Interestingly, HMSNs-S-S-NH-TEG-FA/ $\alpha$ -CD@DOX efficiently inhibited the growth of tumor tissues on nude mice. The mechanism could be interpreted that the [2]rotaxane capping agents on HMSNs prevented DOX release when the nanoparticles were injected into the mouse blood. The folate targeting units could then enable HMSNs-S-S-NH-TEG-FA/ $\alpha$ -CD@DOX to accumulate in tumor tissues followed by DOX release into the cytoplasm triggered by intracellular reductive GSH.

Lastly, we performed histological evaluation of tumor tissues by tunnel apoptosis assay.<sup>53,55</sup> After treatment with HMSNs, DOX, HMSNs@DOX, and HMSNs-S-S-NH-TEG-FA/ $\alpha$ -CD@DOX for 7 and 21 days, relevant tumor tissues were removed from nude mice and frozen-cut into thin sections for histological observation using a tunnel apoptosis assay kit. The tunnel apoptosis assay

kit was utilized to specifically conjugate with the broken double-stranded DNA. As shown in Figure 6d, tumor cells were in good condition after being treated with HMSNs for 7 days. Then, the tumor cells formed more compact structures *in situ* after being treated with HMSNs for 21 days (Figure 6d1). The phenomenon confirmed that, after treatment with bare HMSNs, the amount and activity of the tumor cells were increased *in vivo* over time. In contrast, the growth of tumor cells was inhibited after treatment with DOX, HMSNs@DOX, and HMSNs-S-S-NH-TEG-FA/ $\alpha$ -CD@DOX for 7 days, respectively (Figure 6e–g). Interestingly, the nude mice treated with HMSNs-S-S-NH-TEG-FA/ $\alpha$ -CD@DOX exhibited much better curative effects than those of other groups, showing a lot of apoptotic DNA (in red color) in tumor tissues. In addition, the cell nuclei were also deformed and cracked. The therapy effects of HMSNs@DOX on nude mice were also better than that of pure DOX. The same trends were also observed after treatment for 21 days (Figure 6e1–g1). The results firmly demonstrated that HMSNs-S-S-NH-TEG-FA/ $\alpha$ -CD@DOX could efficiently deliver DOX to tumor cells for inducing apoptosis and cell death *in vivo*.<sup>53,55</sup>

Generally, the limitations inherent to most clinical anticancer chemotherapeutic agents (*e.g.*, DOX) are their severe side effects on normal organs and their lack of tumor selectivity.<sup>56–58</sup> For efficiently curing tumor illness, the current study presented a novel type of intracellular redox-responsive drug delivery system with tumor specificity. After injection into the tail vein of mice, HMSNs-S-S-NH-TEG-FA/ $\alpha$ -CD@DOX could escape from renal clearance, extend its blood circulation time, and selectively pass through the vascular wall *via* enhanced permeability and retention (EPR) effects.<sup>56</sup> The EPR effects are based on leaky vasculature and dysfunctional lymphatic drainage near the tumor sites.<sup>56</sup> Then, the delivery system self-accumulated around the tumor tissues. The FA units functionalized on the surface of HMSNs-S-S-NH-TEG-FA/ $\alpha$ -CD@DOX further facilitated specific internalization of the delivery system within tumor cells *in vivo* through receptor-mediated endocytosis.<sup>46</sup> After that, the loaded DOX within the delivery system was released into the cytoplasm triggered by an intracellular reducing agent, leading to apoptosis and cell death.<sup>58</sup> Previous studies have confirmed that the amount of GSH within tumor cells is about 10<sup>3</sup>-fold higher than that of GSH in the extracellular matrix.<sup>40,41</sup> Indeed, the HMSNs-S-S-NH-TEG-FA/ $\alpha$ -CD@DOX delivery system demonstrated its excellent performance and efficiency in therapeutic treatment on tumor cells with minimal side effects. It is an efficient redox-responsive carrier for controlled drug delivery with tumor specificity *in vitro* and *in vivo*.

## CONCLUSION

In conclusion, we have designed and constructed a biocompatible and intracellular redox-responsive drug



delivery system by immobilizing cleavable [2]rotaxanes onto hollow mesoporous silica nanocontainers connected through disulfide bonds. The [2]rotaxane capping agent was composed of tetraethylene glycol,  $\alpha$ -cyclodextrin, and folic acid. The folate unit could endow the mechanized HMSNs with targeting capability to tumor cells *via* receptor-mediated endocytosis. Doxorubicin-loaded mechanized HMSNs (HMSNs-S-S-NH-TEG-FA/ $\alpha$ -CD@DOX) have been proven to be superb for specifically delivering DOX into tumor cells with minimal side effects *in vitro* and *in vivo*.

## MATERIALS AND METHODS

**Materials.** Chemicals and reagents were purchased from Sigma-Aldrich and used without further purifications. All solvents and inorganic reagents were commercially available.

**General Procedures.**  $^1\text{H}$  NMR and two-dimensional  $^1\text{H}$  NMR were operated on a Bruker BBFO-400 spectrometer. Mass spectrometry was carried out on a ThermoFinnigan LCQ Fleet MS spectrometer. SEM and TEM images were collected on JSM-7100F (JEOL, Japan) and JEM-1400 (JEOL) operated at 100 kV, respectively. The drug release behavior was monitored in real time by a fluorospectrophotometer (RF5301PC, Shimadzu, Japan) using a 1 cm quartz cell. Confocal laser scanning microscopy (LSM 510 Meta, Zeiss Co., Germany) was used to investigate the nanoparticle distribution within cells. Flow cytometry (Coulter Epice XL, Beckman Coulter, USA) was employed to quantitatively determine the percentage of cells internalized with nanoparticles and the amount of endocytosed nanoparticles inside the cells. DNA ladder analysis for tumor cells was performed on a wide mini-sub GT cell (110 V, Biorad Co., USA) and observed by Gel Doc XR+ (Biorad Co., USA). To perform histological examination of tumor tissues, related tissues removed from nude mice were frozen-sliced into thin sections (Leica CM1950, Germany) and observed by CLSM (510 Meta, Germany).

**Synthesis of Compounds.** The syntheses of *S*-(2-aminoethylthio)-2-thiopyridine hydrochloride, *p*-toluenesulfonate-tetraethylene glycol (Tos-TEG-OH), azide glycol (OH-TEG- $\text{N}_3$ ), *p*-toluenesulfonate-tetraethylene glycol-azide (Tos-TEG- $\text{N}_3$ ), and propargylamine-functionalized folic acid (FA-C $\equiv$ C) are described in the SI. They were characterized by  $^1\text{H}$  NMR and MS (see SI for details).

**Preparation of HMSNs.** To obtain HMSNs, silica dioxide ( $\text{SiO}_2$ ) nanoparticles and surfactant CTAB (hexadecyltrimethylammonium bromide)-covered  $\text{SiO}_2$ @CTAB- $\text{SiO}_2$  core/shell nanoparticles were synthesized according to previous reports with some modifications.<sup>34</sup> Then, sodium carbonate ( $\text{Na}_2\text{CO}_3$ ) was employed to selectively etch the  $\text{SiO}_2$  core at 50  $^\circ\text{C}$ . Finally, HMSNs were prepared after extracting CTAB from the nanoparticles using a methanol/hydrochloric acid mixture solution. The detailed procedures are presented in the SI.

**Preparation of Mechanized HMSNs.** To synthesize mechanized HMSNs, functional [2]rotaxane was immobilized onto the orifices of HMSNs. Briefly, the preparation procedures were divided into four steps.

First, HMSNs were modified with sulfhydryl groups.<sup>11,12</sup> Synthesized HMSNs (0.2 g) were refluxed with anhydrous toluene (50 mL) containing 3-mercaptopropyltrimethoxysilane (0.5 mL) at 60  $^\circ\text{C}$  for 20 h. After centrifugation, the products were extensively washed with acetone and ethanol. The obtained sample was obtained as HMSNs-HS.

Second, HMSNs were functionalized with disulfide bonds.<sup>11</sup> Synthesized HMSNs-HS nanoparticles (0.5 g) were dispersed into an ethanol solution (30 mL) containing acetic acid (1.2 mL). Then, *S*-(2-aminoethylthio)-2-thiopyridine hydrochloride (0.5 g) was added to the solution, and the mixture was stirred at room temperature for another 48 h. The resulting product was washed with ethanol and distilled water three times, respectively, and

DOX delivered by HMSNs-S-S-NH-TEG-FA/ $\alpha$ -CD@DOX could effectively inhibit the growth of tumors. Encouraged by the promising results, in the following studies, we will (1) synthesize degradable HMSNs by doping zinc or iron elements, which may enable the nanoparticles to be excreted from the body after the drug release,<sup>59</sup> and (2) investigate biological response of the nanoparticles with some organs, including immunoresponse, metabolic activities, and excretion behavior, which will help us accumulate proof for future clinical applications.<sup>60</sup>

dried under vacuum at 30  $^\circ\text{C}$  for 12 h. The product was obtained as HMSNs-S-S-NH $_2$ .

Third, HMSNs were grafted with TEG molecules.<sup>22</sup> Synthesized HMSNs-S-S-NH $_2$  nanoparticles (0.5 g) were dispersed into methanol (80 mL) with vigorous stirring at 45  $^\circ\text{C}$  for 6 h. Then, Tos-TEG- $\text{N}_3$  was added to the above solution and the mixture was stirred overnight. The reaction occurred between the toluenesulfonate group of Tos-TEG- $\text{N}_3$  and the  $-\text{NH}_2$  group on the HMSNs-S-S-NH $_2$  nanoparticles. The resulting product was collected by centrifugation. Then, the product was washed with ethanol and distilled water three times, respectively, and dried under vacuum at 30  $^\circ\text{C}$ . The final product was obtained as HMSNs-S-S-NH-TEG- $\text{N}_3$ .

Fourth, HMSNs were functionalized with the [2]rotaxanes. Synthesized HMSNs-S-S-NH-TEG- $\text{N}_3$  nanoparticles (20 mg) and DOX (20 mg) were dispersed into distilled water (12 mL) with stirring for 24 h. After loading DOX, a solution of  $\alpha$ -CD (0.3 g) in distilled water (10 mL) was slowly added to the above solution, which was stirred at 4  $^\circ\text{C}$  for 24 h. The  $\alpha$ -CD ring was threaded onto the TEG chain of HMSNs-S-S-NH-TEG- $\text{N}_3$  *via* a hydrophobic interaction.<sup>22</sup> Then, FA-C $\equiv$ C (10 mg) in *N,N*-dimethylformamide (DMF) (2 mL),  $\text{CuSO}_4$  (2 mg), and ascorbic acid (5 mg) in distilled water (2 mL) were sequentially added to the above mixture solution. The click reaction was carried out under  $\text{N}_2$  protection for 24 h.<sup>22,29</sup> After centrifugation, the sample was washed with DMF and distilled water four times, respectively, followed by vacuum freeze-drying. The resulting product was obtained as HMSNs-S-S-NH-TEG-FA/ $\alpha$ -CD@DOX. When DOX was not added in the fourth step, the resulting product was obtained as HMSNs-S-S-NH-TEG-FA/ $\alpha$ -CD.

When DOX was replaced by FITC (10 mg) in the fourth step, the resulted product was obtained as HMSNs-S-S-NH-TEG-FA/ $\alpha$ -CD@FITC. The preparation of mechanized HMSNs was monitored by FITR, BET, SEM, TME, and TGA.

**Redox-Responsive Drug Release by HMSNs-S-S-NH-TEG-FA/ $\alpha$ -CD.** To investigate redox-responsive drug release of HMSNs-S-S-NH-TEG-FA/ $\alpha$ -CD under intracellular reductive GSH, the anticancer drug DOX was used as a model therapeutic agent.<sup>38,39</sup> DOX can generate emission fluorescence at 545 nm under the excitation wavelength of 480 nm. The real-time and long-term drug release behavior of HMSNs-S-S-NH-TEG-FA/ $\alpha$ -CD@DOX was monitored by fluorospectrophotometer and was illustrated in the SI.

**Cell Culture.** HeLa cells and human endothelial cells were cultured with DMEM and RPMI1640 medium containing 10% FBS (Gibco), penicillin (100  $\text{U mL}^{-1}$ ), and streptomycin (100  $\mu\text{g mL}^{-1}$ ) at 37  $^\circ\text{C}$  under 5%  $\text{CO}_2$  atmosphere. The cell culture medium was changed every 48 h. Then, HeLa cells were seeded into 24-well plates or cell culture flasks at an initial cell density of  $2 \times 10^4$  cells per  $\text{cm}^2$ . When cell confluence reached around 60–70%, the culture medium was replaced with fresh medium containing samples of HMSNs, HMSNs-S-S-NH-TEG-FA/ $\alpha$ -CD, DOX, and HMSNs-S-S-NH-TEG-FA/ $\alpha$ -CD@DOX, respectively, for the following studies.

**Characterization of Nanoparticle Distribution within HeLa Cells by TEM.** To investigate the nanoparticle distribution within cells, HeLa cells were treated with normal cell culture conditions, HMSNs (70  $\mu\text{g mL}^{-1}$ ), and HMSNs-S-S-NH-TEG-FA/ $\alpha$ -CD



(70  $\mu\text{g mL}^{-1}$ ) for 24 h, respectively. The samples for the TEM observation were prepared according to previous reports.<sup>42,43</sup> Briefly, cells were first collected and fixed with a mixture solution of glutaraldehyde (2% w/v) and paraformaldehyde (2% w/v) at 4 °C for 2 h, followed by washing with cacodylate buffer three times. Then, the samples were postfixed in osmic acid (2%) for 15 min and stained in a uranyl acetate solution for another 15 min. After dehydration in a graded series of ethanol, the samples were incubated with a mixture solution of dehydrated ethanol and Spurr's medium (1:1, v/v) for another 1 h. The samples were kept in a vacuum oven at 60 °C overnight. Finally, the samples were cut into ultrathin sections by a microtome and stained with uranyl acetate on the grid for 5 min. The distribution of HMSNs-S-S-NH-TEG-FA/ $\alpha$ -CD within cells was observed by TEM.

**Characterization of Nanoparticle Distribution within HeLa Cells by CLSM.** To investigate the nanoparticle distribution within cells, HeLa cells were incubated with FITC, HMSNs@FITC, and HMSNs-S-S-NH-TEG-FA/ $\alpha$ -CD@FITC (70  $\mu\text{g mL}^{-1}$ ), respectively.<sup>16,30,32</sup> After culture at 37 °C for 12 and 24 h, respectively, typan blue (200  $\mu\text{g mL}^{-1}$ ) was added into the incubation medium to quench intracellular fluorescence for 10 min. Then, cells were fixed with 2% glutaraldehyde for 20 min and permeabilized with 0.2% Triton X-100 at 4 °C for 2 min. Subsequently, cells were stained with rhodamine-phalloidin (5 U  $\text{mL}^{-1}$ ) at 4 °C overnight. To further observe cell nuclei, cells were stained with Hoechst 33258 (10  $\mu\text{g mL}^{-1}$ ) for 5 min. Finally, the stained samples were mounted with 90% glycerinum. Cell nuclei and intracellular fluorescent nanoparticles were observed by CLSM. In addition, average fluorescence intensity per cell was analyzed by the software Image-Pro Plus 6.0.

**Quantitative Analysis of Nanoparticle Distribution within Different Cells.** To quantify the fraction (percent (%)) of FITC-positive cells of cells that internalized with nanoparticles, flow cytometry was used to determine the percentage of cells internalized with nanoparticles and the amount of endocytosed nanoparticles inside the cells.<sup>30,32</sup> HeLa cells were cultured into a 24-well plate at an initial seeding density of  $2 \times 10^4$  cells  $\text{cm}^{-2}$ . After being treated with nanoparticles (30  $\mu\text{g mL}^{-1}$ ) at 37 °C for 2 and 4 h, respectively, cells were collected, and the extracellular fluorescence was quenched by typan blue (200  $\mu\text{g mL}^{-1}$ ) at room temperature for 10 min. Cells were then washed and resuspended in PBS. Finally, the percentage of cells internalized with nanoparticles and the amount of endocytosed nanoparticles inside the cells were analyzed by flow cytometry.

**Cytotoxicity Assay by MTT.** The culture medium was replaced with fresh medium containing HMSNs, HMSNs-S-S-NH-TEG-FA/ $\alpha$ -CD, DOX, and HMSNs-S-S-NH-TEG-FA/ $\alpha$ -CD@DOX, respectively, when cell confluence reached around 60–70%.<sup>28,32,45</sup> After incubation at 37 °C for 6, 12, and 24 h, respectively, the medium was changed with fresh culture medium. Then, MTT solution (0.1 mL, 5  $\text{mg mL}^{-1}$ ) was added to each well, which were incubated for another 4 h. Finally, MTT-containing medium was removed, and dimethyl sulfoxide (0.5 mL) was added to dissolve formose crystals. After centrifugation, optical density of the solution was measured by the enzyme-linked immunosorbent assay (ELISA) at a wavelength of 490 nm.<sup>28,32,45</sup>

**Cell Apoptosis Assay by CLSM and DNA Ladder Analysis.** HeLa cells were cultured with HMSNs, HMSNs-S-S-NH-TEG-FA/ $\alpha$ -CD, DOX, and HMSNs-S-S-NH-TEG-FA/ $\alpha$ -CD@DOX under the same procedure as mentioned above.<sup>16,17,52</sup> After incubation at 37 °C for 12 and 24 h, respectively, cells were fixed with 2% glutaraldehyde for 20 min and stained with Hoechst 33258 (10  $\mu\text{g mL}^{-1}$ ) for 5 min. Finally, the stained samples were mounted with 90% glycerinum. Cell nuclei were observed by CLSM. Meanwhile, DNA fragmentation assay was also performed. DNA was extracted according to the operation manual of the cell apoptosis DNA ladder isolation kit, followed by identification via gel electrophoresis with 0.8% agarose gel.

**Establishment of Tumor Models on Nude Mice.** Normal nude mice (average weight  $19.3 \pm 0.3$  g) were provided by Xingqiao Hospital of The Third Military Medical University (Chongqing, China) for studies *in vivo*. Animal experiments were carried out according to the Animal Management Rules of the Ministry of Health of the People's Republic of China (Document No. 55, 2001) and the guidelines for the Care and Use of Laboratory Animals of

The Third Military Medical University. HeLa cells (0.2 mL,  $1.5 \times 10^7$  cells  $\text{mL}^{-1}$  in PBS) were injected into subcutaneous tissue of the nude mice.<sup>51–53</sup> After that, all the treated nude mice were observed every day to monitor the sizes of tumors by using a digital caliper. When the tumor size of the mice grew to an average volume of 25  $\text{mm}^3$ , calculated by the formula volume = (tumor length)  $\times$  (tumor width)<sup>2</sup>/2, the mice were used for further studies.<sup>54</sup> The mice with the maximum size and the minimum size of tumors were discarded. Finally, six representative mice were analyzed. Tumor tissues were removed from the bodies of the mice to investigate the initial stage of the tumor morphology.

**Treatment of Nude Mice Bearing Tumor.** In this study, 60 mice bearing lipoma tumor were divided into five groups, which were intravenously injected with saline, HMSNs, HMSNs-S-S-NH-TEG-FA/ $\alpha$ -CD, DOX, and HMSNs-S-S-NH-TEG-FA/ $\alpha$ -CD@DOX, respectively, three times per week.<sup>51–53</sup> The mice treated with saline (100  $\mu\text{L}$ ) were used as the control group. The mice treated with HMSNs-S-S-NH-TEG-FA/ $\alpha$ -CD@DOX were injected with a dose of  $\sim 0.1$  mg per animal (100  $\mu\text{L}$ , 1  $\text{mg mL}^{-1}$ ) each time, which is equivalent to a DOX dose of  $\sim 0.02$  mg per animal (100  $\mu\text{L}$ , 0.2  $\text{mg mL}^{-1}$ ). The concentrations used for the groups treated with HMSNs and HMSNs-S-S-NH-TEG-FA/ $\alpha$ -CD were the same as that of HMSNs-S-S-NH-TEG-FA/ $\alpha$ -CD@DOX. When saline and nanoparticles were injected, the tumor size and mice weight were measured by a digital caliper and digital calculation balance, respectively. After treatment for 1 week and 3 weeks, respectively, related mice were sacrificed, and the tumor tissues were removed from the bodies in order to investigate the morphology and use for further studies.<sup>53,55</sup>

**Evaluation of Cell Apoptosis in Tumor Tissues.** To perform histological examination of tumor tissues in mice, the tumor was removed from the nude mice and frozen-sliced into thin sections.<sup>53,55</sup> All the sections were immobilized onto glass slides via glue, fixed with 4% paraformaldehyde for 1 h, and washed with PBS two times. After that, the samples were permeabilized with 0.2% Triton X-100 at 4 °C for 2 min. Subsequently, cells were stained with tunnel staining reagent (50  $\mu\text{L}$ , rhodamine B-labeled tunnel apoptosis assay kit) at 37 °C for another 1 h. For nucleus visualization, cells were stained with Hoechst 33258 (10  $\mu\text{g mL}^{-1}$ ) for 10 min. Finally, the stained samples were mounted with 90% glycerinum. Cell nuclei and apoptotic DNA were observed by CLSM.

**Conflict of Interest:** The authors declare no competing financial interest.

**Supporting Information Available:** Additional synthesis and characterizations; <sup>1</sup>H NMR spectra and mass spectra of functional molecules; morphologies of SiO<sub>2</sub> and SiO<sub>2</sub>@CTAB nanoparticles; BET nitrogen adsorption/desorption isotherms and BJH pore size analysis of nanoparticles; FTIR spectra, fluorescence spectra, and TGA curves of nanoparticles; release profiles of DOX from mechanized HMSNs under simulated endosome conditions; cytocompatibility analysis of nanoparticles, TEM images of endocytosed nanoparticles within cells; mean fluorescence intensity per cell; fluorescence intensity of nanoparticles after incubation with FBS-FITC/DEME cell culture medium; distribution of nanoparticles after incubation with proteins; cytotoxicity assay of anticancer drug and drug-loaded nanoparticles; mouse weight survey. This material is available free of charge via the Internet at <http://pubs.acs.org>.

**Acknowledgment.** This work was financially supported by the Singapore National Research Foundation Fellowship (NRF2009NRF-RF001-015), Singapore National Research Foundation CREATE Program—Singapore Peking University Research Centre for a Sustainable Low-Carbon Future, and the NTU-A\*Star Centre of Excellence for Silicon Technologies (A\*Star SERC No. 112 351 0003). This work was also partially sponsored by Natural Science Foundation of China (21274169 and 31200712). Z.L. is grateful for the SEM characterizations from Ms. K. T. Nguyen.

## REFERENCES AND NOTES

1. Ferlay, J.; Shin, H. R.; Bray, F.; Forman, D.; Mathers, C.; Parkin, D. M. Estimates of Worldwide Burden of Cancer in 2008: GLOBOCAN 2008. *Int. J. Cancer* **2010**, *127*, 2893–2917.

2. Peer, D.; Karp, J. M.; Hong, S.; Farokhzad, O. C.; Margalit, R.; Langer, R. Nanocarriers as an Emerging Platform for Cancer Therapy. *Nat. Nanotechnol.* **2007**, *2*, 751–760.
3. Bourzac, K. Nanotechnology: Carrying Drugs. *Nature* **2012**, *491*, S58–S60.
4. Ashley, C. E.; Carnes, E. C.; Phillips, G. K.; Padilla, D.; Durfee, P. N.; Brown, P. A.; Hanna, T. N.; Liu, J.; Phillips, B.; Carter, M. B.; et al. The Targeted Delivery of Multicomponent Cargos to Cancer Cells by Nanoporous Particle-Supported Lipid Bilayers. *Nat. Mater.* **2011**, *10*, 389–397.
5. Ambrogio, M. W.; Thomas, C. R.; Zhao, Y.; Zink, J. I.; Stoddart, J. F. Mechanized Silica Nanoparticles: A New Frontier in Theranostic Nanomedicine. *Acc. Chem. Res.* **2011**, *44*, 903–913.
6. Tarn, D.; Ashley, C. E.; Xue, M.; Carnes, E. C.; Zink, J. I.; Brinker, C. J. Mesoporous Silica Nanoparticle Nanocarriers: Biofunctionality and Biocompatibility. *Acc. Chem. Res.* **2013**, *46*, 792–801.
7. Slowing, I. I.; Vivero-Escoto, J. L.; Wu, C. W.; Lin, V. S. Mesoporous Silica Nanoparticles as Controlled Release Drug Delivery and Gene Transfection Carriers. *Adv. Drug Delivery Rev.* **2008**, *60*, 1278–1288.
8. Vallet-Regí, M.; Balas, F.; Arcos, D. Mesoporous Materials for Drug Delivery. *Angew. Chem., Int. Ed.* **2007**, *46*, 7548–7558.
9. Wang, Y.; Wang, K.; Zhao, J.; Liu, X.; Bu, J.; Yan, X.; Huang, R. Multifunctional Mesoporous Silica-Coated Graphene Nanosheet Used for Chemo-Photothermal Synergistic Targeted Therapy of Glioma. *J. Am. Chem. Soc.* **2013**, *135*, 4799–4804.
10. Sreejith, S.; Ma, X.; Zhao, Y. L. Graphene Oxide Wrapping on Squaraine-Loaded Mesoporous Silica Nanoparticles for Bioimaging. *J. Am. Chem. Soc.* **2012**, *134*, 17346–17349.
11. Sun, X.; Zhao, Y.; Lin, V. S.; Slowing, I. I.; Trewyn, B. G. Luciferase and Luciferin Co-Immobilized Mesoporous Silica Nanoparticle Materials for Intracellular Biocatalysis. *J. Am. Chem. Soc.* **2011**, *133*, 18554–18557.
12. Giri, S.; Trewyn, B. G.; Stellmaker, M. P.; Lin, V. S. Stimuli-Responsive Controlled-Release Delivery System Based on Mesoporous Silica Nanorods Capped with Magnetic Nanoparticles. *Angew. Chem., Int. Ed.* **2005**, *44*, 5038–5044.
13. Lai, C. Y.; Trewyn, B. G.; Jeftinija, D. M.; Aznar, E.; Marcos, M. D.; Martínez-Mañez, R.; Sancenón, F.; Soto, J.; Amorós, P.; Guillem, C. pH- and Photo-Switched Release of Guest Molecules from Mesoporous Silica Supports. *J. Am. Chem. Soc.* **2009**, *131*, 6833–6843.
14. Pan, L.; He, Q.; Liu, J.; Chen, Y.; Ma, M.; Zhang, L.; Shi, J. Nuclear-Targeted Drug Delivery of TAT Peptide-Conjugated Monodisperse Mesoporous Silica Nanoparticles. *J. Am. Chem. Soc.* **2012**, *134*, 5722–5725.
15. Liu, J.; Stace-Naughton, A.; Jiang, X.; Brinker, C. J. Porous Nanoparticle Supported Lipid Bilayers (Protocells) as Delivery Vehicles. *J. Am. Chem. Soc.* **2009**, *131*, 1354–1355.
16. Zhang, J.; Yuan, Z. F.; Wang, Y.; Chen, W. H.; Luo, G. F.; Cheng, S. X.; Zhuo, R. X.; Zhang, X. Z. Multifunctional Envelope-Type Mesoporous Silica Nanoparticles for Tumor-Triggered Targeting Drug Delivery. *J. Am. Chem. Soc.* **2013**, *135*, 5068–5073.
17. Xiong, M. H.; Bao, Y.; Yang, X. Z.; Wang, Y. C.; Sun, B.; Wang, J. Lipase-Sensitive Polymeric Triple-Layered Nanogel for “On-Demand” Drug Delivery. *J. Am. Chem. Soc.* **2012**, *134*, 4355–4362.
18. Liu, J.; Jiang, X.; Ashley, C.; Brinker, C. J. Electrostatically Mediated Liposome Fusion and Lipid Exchange with a Nanoparticle-Supported Bilayer for Control of Surface Charge, Drug Containment, and Delivery. *J. Am. Chem. Soc.* **2009**, *131*, 7567–7569.
19. Zhao, Y.; Li, Z.; Kabehie, S.; Botros, Y. Y.; Stoddart, J. F.; Zink, J. I. pH-Operated Nanopistons on the Surfaces of Mesoporous Silica Nanoparticles. *J. Am. Chem. Soc.* **2010**, *132*, 13016–13025.
20. Thomas, C. R.; Ferris, D. P.; Lee, J. H.; Choi, E.; Cho, M. H.; Kim, E. S.; Stoddart, J. F.; Shin, J. S.; Cheon, J.; Zink, J. I. Non-invasive Remote-Controlled Release of Drug Molecules *in Vitro* Using Magnetic Actuation of Mechanized Nanoparticles. *J. Am. Chem. Soc.* **2010**, *132*, 10623–10625.
21. Du, L.; Liao, S.; Khatib, H. A.; Stoddart, J. F.; Zink, J. I. Controlled-Access Hollow Mechanized Silica Nanocontainers. *J. Am. Chem. Soc.* **2009**, *131*, 15136–15142.
22. Patel, K.; Angelos, S.; Dichtel, W. R.; Coskun, A.; Yang, Y. W.; Zink, J. I.; Stoddart, J. F. Enzyme-Responsive Snap-Top Covered Silica Nanocontainers. *J. Am. Chem. Soc.* **2008**, *130*, 2382–2383.
23. Liu, J.; Bu, W.; Pan, L.; Shi, J. NIR-Triggered Anticancer Drug Delivery by Upconverting Nanoparticles with Integrated Azobenzene-Modified Mesoporous Silica. *Angew. Chem., Int. Ed.* **2013**, *52*, 4375–4379.
24. Casasús, R.; Climent, E.; Marcos, M. D.; Martínez-Mañez, R.; Sancenón, F.; Soto, J.; Amorós, P.; Cano, J.; Ruiz, E. Dual Aperture Control on pH- and Anion-Driven Supramolecular Nanoscopic Hybrid Gate-Like Ensembles. *J. Am. Chem. Soc.* **2008**, *130*, 1903–1917.
25. Park, C.; Lee, K.; Kim, C. Photoresponsive Cyclodextrin-Covered Nanocontainers and Their Sol-Gel Transition Induced by Molecular Recognition. *Angew. Chem., Int. Ed.* **2009**, *48*, 1275–1278.
26. Hernandez, R.; Tseng, H. R.; Wong, J. W.; Stoddart, J. F.; Zink, J. I. An Operational Supramolecular Nanovalve. *J. Am. Chem. Soc.* **2004**, *126*, 3370–3371.
27. Nguyen, T. D.; Tseng, H. R.; Celestre, P. C.; Flood, A. H.; Liu, Y.; Stoddart, J. F.; Zink, J. I. A Reversible Molecular Valve. *Proc. Natl. Acad. Sci. U.S.A.* **2005**, *102*, 10029–10034.
28. Zhang, Q.; Liu, F.; Nguyen, K. T.; Ma, X.; Wang, X. J.; Xing, B. G.; Zhao, Y. L. Multifunctional Mesoporous Silica Nanoparticles for Cancer-Targeted and Controlled Drug Delivery. *Adv. Funct. Mater.* **2012**, *22*, 5144–5156.
29. Yan, H.; Teh, C.; Sreejith, S.; Zhu, L.; Kwok, A.; Fang, W.; Ma, X.; Nguyen, K. T.; Korzh, V.; Zhao, Y. L. Functional Mesoporous Silica Nanoparticles for Photothermal-Controlled Drug Delivery *in Vivo*. *Angew. Chem., Int. Ed.* **2012**, *51*, 8373–8377.
30. Luo, Z.; Cai, K. Y.; Hu, Y.; Zhang, B. L.; Xu, D. Cell-Specific Intracellular Anticancer Drug Delivery from Mesoporous Silica Nanoparticles with pH Sensitivity. *Adv. Healthcare Mater.* **2012**, *1*, 321–325.
31. Hu, Y.; Cai, K. Y.; Luo, Z.; Jandt, K. D. Layer-by-Layer Assembly of  $\beta$ -Estradiol Loaded Mesoporous Silica Nanoparticles on Titanium Substrates and Its Implication for Bone Homeostasis. *Adv. Mater.* **2010**, *22*, 4146–4150.
32. Luo, Z.; Cai, K. Y.; Hu, Y.; Zhao, L.; Liu, P.; Duan, L.; Yang, W. Mesoporous Silica Nanoparticles End-Capped with Collagen: Redox-Responsive Nanoreservoirs for Targeted Drug Delivery. *Angew. Chem., Int. Ed.* **2011**, *50*, 640–643.
33. Ebright, Y. W.; Chen, Y.; Kim, Y.; Ebright, R. H. S-[2-(4-Azidosalicylamido)ethylthio]-2-thiopyridine: Radioiodinatable, Cleavable, Photoactivatable Cross-Linking Agent. *Bioconjugate Chem.* **1996**, *7*, 380–384.
34. Fang, X.; Chen, C.; Liu, Z.; Liu, P.; Zheng, N. A Cationic Surfactant Assisted Selective Etching Strategy to Hollow Mesoporous Silica Spheres. *Nanoscale* **2011**, *3*, 1632–1639.
35. Lu, J.; Liong, M.; Zink, J. I.; Tamanoi, F. Mesoporous Silica Nanoparticles as a Delivery System for Hydrophobic Anticancer Drugs. *Small* **2007**, *3*, 1341–1346.
36. Papat, A.; Ross, B. P.; Liu, J.; Jambhrunkar, S.; Kleitz, F.; Qiao, S. Z. Enzyme-Responsive Controlled Release of Covalently Bound Prodrug from Functional Mesoporous Silica Nanospheres. *Angew. Chem., Int. Ed.* **2012**, *51*, 12486–12489.
37. Wang, X.; Chen, H. R.; Zheng, Y.; Ma, M.; Chen, Y.; Zhang, K.; Zeng, D.; Shi, J. L. Au-Nanoparticle Coated Mesoporous Silica Nanocapsule-Based Multifunctional Platform for Ultrasound Mediated Imaging, Cytoclastin and Tumor Ablation. *Biomaterials* **2013**, *34*, 2057–2068.
38. Cui, Y.; Dong, H.; Cai, X.; Wang, D.; Li, Y. Mesoporous Silica Nanoparticles Capped with Disulfide-Linked PEG Gatekeepers for Glutathione-Mediated Controlled Release. *ACS Appl. Mater. Interfaces* **2012**, *4*, 3177–3183.
39. Lai, J.; Shah, B. P.; Garfunkel, E.; Lee, K. B. Versatile Fluorescence Resonance Energy Transfer-Based Mesoporous Silica Nanoparticles for Real-Time Monitoring of Drug Release. *ACS Nano* **2013**, *7*, 2741–2750.

40. Verma, A.; Simard, J. M.; Worrall, J. W.; Rotello, V. M. Tunable Reactivation of Nanoparticle-Inhibited  $\beta$ -Galactosidase by Glutathione at Intracellular Concentrations. *J. Am. Chem. Soc.* **2004**, *126*, 13987–13991.
41. Kim, H.; Kim, S.; Park, C.; Lee, H.; Park, H. J.; Kim, C. Glutathione-Induced Intracellular Release of Guests from Mesoporous Silica Nanocontainers with Cyclodextrin Gatekeepers. *Adv. Mater.* **2010**, *22*, 4280–4283.
42. Schrand, A. M.; Schlager, J. J.; Dai, L.; Hussain, S. M. Preparation of Cells for Assessing Ultrastructural Localization of Nanoparticles with Transmission Electron Microscopy. *Nat. Protoc.* **2010**, *5*, 744–757.
43. Cai, K. Y.; Hou, Y.; Hu, Y.; Zhao, L.; Luo, Z.; Shi, Y.; Lai, M.; Yang, W.; Liu, P. Correlation of the Cytotoxicity of TiO<sub>2</sub> Nanoparticles with Different Particle Sizes on a Sub-200-nm Scale. *Small* **2011**, *7*, 3026–3031.
44. Colbert, J. D.; Matthews, S. P.; Miller, G.; Watts, C. Diverse Regulatory Roles for Lysosomal Proteases in the Immune Response. *Eur. J. Immunol.* **2009**, *39*, 2955–2956.
45. Luo, Z.; Cai, K. Y.; Hu, Y.; Li, J. H.; Ding, X. W.; Zhang, B. L.; Xu, D. W.; Yang, W. H.; Liu, P. Redox-Responsive Molecular Nanoreservoirs for Controlled Intracellular Anticancer Drug Delivery Based on Magnetic Nanoparticles. *Adv. Mater.* **2012**, *24*, 431–435.
46. Liong, M.; Lu, J.; Kovochich, M.; Xia, T.; Ruehm, S. G.; Nel, A. E.; Tamanoi, F.; Zink, J. I. Multifunctional Inorganic Nanoparticles for Imaging, Targeting, and Drug Delivery. *ACS Nano* **2008**, *2*, 889–896.
47. Wang, F.; Wang, Y. C.; Dou, S.; Xiong, M. H.; Sun, T. M.; Wang, J. Doxorubicin-Tethered Responsive Gold Nanoparticles Facilitate Intracellular Drug Delivery for Overcoming Multi-drug Resistance in Cancer Cells. *ACS Nano* **2011**, *5*, 3679–3692.
48. Huang, I. P.; Sun, S. P.; Cheng, S. H.; Lee, C. H.; Wu, C. Y.; Yang, C. S.; Lo, L. W.; Lai, Y. K. Enhanced Chemotherapy of Cancer Using pH-Sensitive Mesoporous Silica Nanoparticles to Antagonize P-Glycoprotein-Mediated Drug Resistance. *Mol. Cancer Ther.* **2011**, *10*, 761–769.
49. Tewey, K. M.; Rowe, T. C.; Yang, L.; Halligan, B. D.; Liu, L. F. Adriamycin-Induced DNA Damage Mediated by Mammalian DNA Topoisomerase II. *Science* **1984**, *226*, 466–468.
50. Wang, Y.; Arriaga, E. A. Monitoring Incorporation, Transformation and Subcellular Distribution of N-I-Leucyl-Doxorubicin in Uterine Sarcoma Cells Using Capillary Electrophoretic Techniques. *Cancer Lett.* **2008**, *262*, 123–132.
51. Dhar, S.; Kolishetti, N.; Lippard, S. J.; Farokhzad, O. C. Targeted Delivery of a Cisplatin Prodrug for Safer and More Effective Prostate Cancer Therapy *in Vivo*. *Proc. Natl. Acad. Sci. U.S.A.* **2011**, *108*, 1850–1855.
52. Meng, H.; Mai, W. X.; Zhang, H.; Xue, M.; Xia, T.; Lin, S.; Wang, X.; Zhao, Y.; Ji, Z.; Zink, J. I.; *et al.* Codelivery of an Optimal Drug/siRNA Combination Using Mesoporous Silica Nanoparticles to Overcome Drug Resistance in Breast Cancer *in Vitro* and *in Vivo*. *ACS Nano* **2013**, *7*, 994–1005.
53. Singh, N.; Karambelkar, A.; Gu, L.; Lin, K.; Miller, J. S.; Chen, C. S.; Sailor, M. J.; Bhatia, S. N. Bioresponsive Mesoporous Silica Nanoparticles for Triggered Drug Release. *J. Am. Chem. Soc.* **2011**, *133*, 19582–19585.
54. Yang, K.; Xu, H.; Cheng, L.; Sun, C.; Wang, J.; Liu, Z. *In Vitro* and *in Vivo* Near-Infrared Photothermal Therapy of Cancer Using Polypyrrole Organic Nanoparticles. *Adv. Mater.* **2012**, *24*, 5586–5592.
55. Idris, N. M.; Gnanasammandhan, M. K.; Zhang, J.; Ho, P. C.; Mahendran, R.; Zhang, Y. *In Vivo* Photodynamic Therapy Using Upconversion Nanoparticles as Remote-Controlled Nanotransducers. *Nat. Med.* **2012**, *18*, 1580–1585.
56. Farokhzad, O. C.; Langer, R. Impact of Nanotechnology on Drug Delivery. *ACS Nano* **2005**, *3*, 16–20.
57. Ferrari, M. Cancer Nanotechnology: Opportunities and Challenges. *Nat. Rev. Cancer* **2005**, 161–171.
58. Deng, C.; Jiang, Y. J.; Cheng, R.; Meng, F. H.; Zhong, Z. Y. Biodegradable Polymeric Micelles for Targeted and Controlled Anticancer Drug Delivery: Promises, Progress and Prospects. *Nano Today* **2012**, *7*, 467–480.
59. Zhang, S.; Chu, Z.; Yin, C.; Zhang, C.; Lin, G.; Li, Q. Controllable Drug Release and Simultaneously Carrier Decomposition of SiO<sub>2</sub>-Drug Composite Nanoparticles. *J. Am. Chem. Soc.* **2013**, *135*, 5709–5716.
60. Andón, F. T.; Fadeel, B. Programmed Cell Death: Molecular Mechanisms and Implications for Safety Assessment of Nanomaterials. *Acc. Chem. Res.* **2013**, *46*, 733–742.